SUPPLEMENTARY MATERIALS AND METHODS

Image acquisition

As previously described (1), all MRI scans were acquired using the same 3T Siemens Tim Trio whole-body scanner and 32-channel head coil at the Hospital of the University of Pennsylvania.

Structural MRI:

Prior to functional MRI acquisitions, a 5-min magnetization-prepared, rapid acquisition gradient-echo T1-weighted (MPRAGE) image (TR =1810ms; TE=3.51ms; TI=1100ms, FOV=180 x 240mm^2, matrix=192 x 256, effective voxel resolution=0.9 x 0.9 x 1mm^3) was acquired.

Functional MRI:

We used one resting-state and two task-based (i.e., *n*-back and emotion recognition) fMRI scans as part of this study. All fMRI scans were acquired with the same single-shot, interleaved multi-slice, gradient-echo, echo planar imaging (GE-EPI) sequence sensitive to BOLD contrast with the following parameters: TR = 3000 ms; TE = 32 ms; flip angle = 90°; FOV = 192 x 192 mm^2; matrix = 64 x 64; 46 slices; slice thickness/gap = 3/0 mm, effective voxel resolution = 3.0 x 3.0 x 3.0 mm^3. Resting-state scans had 124 volumes, while the *n*-back and emotion recognition scans had 231 and 210 volumes, respectively. Further details regarding the *n*-back (2) and emotion recognition (3) tasks have been described in prior publications.

Field map:

A B0 field map was derived for application of distortion correction procedures, using a double-echo, gradient-recalled echo (GRE) sequence: TR = 1000ms; TE1 = 2.69 ms; TE2 =

5.27 ms; 44 slices; slice thickness/gap = 4/0 mm; FOV = 240 mm; effective voxel resolution = 3.8 x 3.8 x 4 mm.

Image processing

The structural images were processed using FreeSurfer (version 5.3) to allow for the projection of functional time series to the cortical surface (4). Functional images were processed using a top-performing preprocessing pipeline implemented using the eXtensible Connectivity Pipeline (XCP) Engine (5), which includes tools from FSL (6, 7) and AFNI (8). This pipeline included 1) correction for distortions induced by magnetic field inhomogeneity using FSL's FUGUE utility, 2) removal of the initial volumes of each acquisition (i.e., 4 volumes for resting-state fMRI and 6 volumes for emotion recognition task fMRI), 3) realignment of all volumes to a selected reference volume using FSL's MCFLIRT, 4) interpolation of intensity outliers in each voxel's time series using AFNI's 3dDespike utility, 5) demeaning and removal of any linear or quadratic trends, and 6) co-registration of functional data to the high-resolution structural image using boundary-based registration. Images were de-noised using a 36-parameter confound regression model that has been shown to minimize associations with motion artifact while retaining signals of interest in distinct sub-networks. This model included the six framewise estimates of motion, the mean signal extracted from eroded white matter and cerebrospinal fluid compartments, the mean signal extracted from the entire brain, the derivatives of each of these nine parameters, and quadratic terms of each of the nine parameters and their derivatives. Both the BOLD-weighted time series and the artifactual model time series were temporally filtered using a first-order Butterworth filter with a passband between 0.01 and 0.08 Hz to avoid mismatch in the temporal domain (9). Furthermore, to derive ‘‘pseudo-resting state’’ time series that were comparable across runs, the task activation model was regressed from n-back or emotion recognition fMRI data (10). The task activation model and the nuisance matrix were regressed out using AFNI's 3dTproject.

For each modality, the fMRI time series of each individual were projected to each subject's FreeSurfer surface reconstruction and smoothed on the surface with a 6-mm full-width half-maximum (FWHM) kernel. The smoothed data was projected to the *fsaverage5* template, which has 10,242 vertices on each hemisphere (18,715 vertices in total after removing the medial wall). Finally, we concatenated the three fMRI acquisitions, yielding time series of length 27 minutes, 45 seconds (555 time points) in total.

As in prior work, we removed vertices with low signal-to-noise ratio (SNR) (11-13). To calculate a whole-brain SNR map, we extracted the first frame of acquisition (post steady-state magnetization) of each of the three runs for all participants. Next, we normalized each image to a mode of 1,000 and then averaged all of these images; this average image was further normalized to a mode of 1,000. A mean BOLD signal of 800 or less represents a substantial attenuation of signal (13); applying this threshold resulted in the exclusion of low SNR locations, which were primarily located in orbitofrontal cortex and ventral temporal cortex. Within this mask, 17,734 vertices were included in subsequent analyses.

Regularized non-negative matrix factorization

As previously described in detail (14), we used non-negative matrix factorization (NMF) (15) to derive individualized functional networks. NMF factors the data by positively weighting cortical elements that covary; the algorithm yields a highly specific and reproducible parts-based representation (15, 16). Our approach was enhanced by a group sparsity consensus regularization term that preserves inter-individual correspondence, as well as a data locality regularization term that makes the decomposition robust to imaging noise, improves spatial smoothness, and enhances functional coherence of subject-specific functional networks (see Li *et al*., 2017 (14) for method details; see also: https://github.com/hmlicas/Collaborative_Brain_Decomposition). Because NMF requires inputs to be nonnegative values, we re-scaled the data by shifting time series of each vertex linearly to

ensure that all values were positive (14). To avoid features in greater numeric ranges dominating those in a smaller numeric range, we further normalized the time series by its maximum value so that all the time points have values in the range [0, 1].

Given a group of *n* subjects, each having fMRI data $X^i \in R^{T\times S}, i = 1, \dots, n$, consisting of *S* vertices and *T* time points, we aimed to find *K* non-negative functional networks $V^i = (V^i_{s,k}) \in R^{S\times K}$ and their corresponding time series $U^i = (U^i_{t,k}) \in R^{T\times K}$ for each subject, such that

$$X^i \approx U^i\left(V^i\right)' + E^i, s.t. U^i, V^i \geq 0, \forall 1 \leq i \leq n,$$

where $(V^i)'$ is the transpose of (V^i), and E^i is independently and identically distributed (i.i.d) residual noise following Gaussian distribution with a probability density function of $g(x) = \frac{1}{\sqrt{2\pi}\sigma} e^{-\frac{x^2}{2\sigma^2}}$. Both U^i and V^i were constrained to be non-negative so that each functional network does not contain any anti-correlated functional units (15). A group consensus regularization term was applied to ensure inter-individual correspondence, which was implemented as a scale-invariant group sparsity term on each column of V^i and formulated as

$$R_c = \sum_{k=1}^{K} \left\| \widetilde{V^{1,\dots,n}_{\cdot,k}} \right\|_{2,1} = \sum_{k=1}^{K} \frac{\sum_{s=1}^{S}(\sum_{i=1}^{n}(V^i_{s,k})^2)^{1/2}}{(\sum_{s=1}^{S}\sum_{i=1}^{n}(V^i_{s,k})^2)^{1/2}}.$$

The data locality regularization term was applied to encourage spatial smoothness and coherence of the functional networks using graph regularization techniques (17). The data locality regularization term was formulated as

$$R^i_M = Tr((V^i)'L^i_M V^i),$$

where $L^i_M = D^i_M - W^i_M$ is a Laplacian matrix for subject *i*, W^i_M is a pairwise affinity matrix to measure spatial closeness or functional similarity between different vertices, and D^i_M is its corresponding degree matrix. The affinity between each pair of spatially connected vertices (i.e., vertices *a* and *b*) was calculated as $\left(1 + corr\left(X^i_{\cdot,a}, X^i_{\cdot,b}\right)\right)/2$, where $corr(X^i_{\cdot,a}, X^i_{\cdot,b})$ is the Pearson correlation coefficient between time series $X^i_{\cdot,a}$ and $X^i_{\cdot,b}$, and others were set to zero so that W^i_M

had a sparse structure. We identified subject specific functional networks by optimizing a joint model with integrated data fitting and regularization terms formulated by

$$\min_{(U^i, V^i)} \sum_{i=1}^{n} \left\| X^i - U^i (V^i)' \right\|_F^2 + \lambda_M \sum_{i=1}^{n} R_M^i + \lambda_c R_c$$

$$s.t. U^i, V^i \geq 0, \left\| V_{.,k}^i \right\|_\infty = 1, \forall 1 \leq k \leq K, \forall 1 \leq i \leq n$$

where $\lambda_M = \beta \times \frac{T}{K \times n_M}$ and $\lambda_c = \alpha \cdot \frac{n \cdot T}{K}$ are used to balance the data fitting, data locality, and group consensus regularization terms, n_M is the number of neighboring vertices, α and β are free parameters. Here, we used the same parameter settings as those used in prior validation studies (14).

Defining individualized networks

Our approach for defining individualized networks included three steps (**Figure 1**). The first two steps yielded a consensus group atlas. In the third step, this group atlas was used to define individualized networks for each participant. The whole-brain was decomposed into 17 networks for correspondence with commonly used atlases and prior work (18-21).

Step 1: Group network initialization

Although individuals exhibit distinct network topography, they are also broadly consistent (22, 23). Therefore, we first generated a group atlas and used this group atlas as an initialization to define individualized networks. By doing so, we ensured spatial correspondence across all subjects. This strategy has been applied in prior work (18, 19, 21). To avoid the group atlas being driven by outliers and to reduce the computational memory cost, a bootstrap strategy was utilized to perform the group-level decomposition multiple times on a subset of randomly selected subjects. Subsequently, the resulting decomposition results were fused to obtain one robust initialization that is highly reproducible. As in prior work (14), we randomly selected 100 subjects and temporally concatenated their time series, resulting in a time series matrix with

55,500 rows (time-points) and 17,734 columns (vertices). The choice of sub-sample size did not impact results (sub-samples of 100, 200, and 300 were previously evaluated (21)). We applied the above-mentioned regularized non-negative matrix factorization method with a random non-negative initialization to decompose this matrix (15). A group-level network loading matrix *V* was acquired, which had 17 rows and 17,734 columns. Each row of this matrix represents a functional network, while each column represents the loadings of a given cortical vertex. This procedure was repeated 50 times, each time with a different subset of subjects (14); this yielded 50 different group atlases.

Step 2: Group network consensus

Next, we used spectral clustering to combine the 50 group network atlases into one robust and highly reproducible group network atlas (14). Specifically, we concatenated the 50 group parcellations together across networks and acquired a matrix with 850 rows (i.e., functional networks, abbreviated as FN) and 17,734 columns (i.e., vertices). Inter-network similarity was calculated as

$$S_{ij} = exp\left(-\frac{d_{ij}^2}{\sigma^2}\right),$$

where $d_{ij} = 1 - corr(FN_i, FN_j)$, $corr(FN_i, FN_j)$ is the Pearson correlation coefficient between FN_i and FN_j, and σ is the median of d_{ij} across all possible pairs of FNs. Then, we applied a normalized-cuts (17) based spectral clustering method to group the 850 FNs into 17 clusters. For each cluster, the FN with the highest overall similarity with all other FNs within the same cluster was selected as the most representative. The final group network atlas was composed of the representatives of these 17 clusters.

Step 3: Individualized networks.

In this final step, we derived each individual's specific network atlas using regularized

NMF based on the acquired group networks (17 x 17,734 loading matrix) as initialization and each individual's specific fMRI times series (555 x 17,734 matrix). See Li *et al.*, 2017 (14) for optimization details. This procedure yielded a loading matrix V (17 x 17,734 matrix) for each participant, where each row is a functional network, each column is a vertex, and the value quantifies the extent that each vertex belongs to each network. This probabilistic network definition (or soft partition) can be converted into a discrete network definition (or hard partition) for visual display by labeling each vertex according to its highest loading.

Sensitivity analyses

First, we investigated if age impacted the ability to classify sex based on multivariate patterns of topography. We divided our sample into 3 tertiles based on age: tertile 1 (n=231; 8.2 - 14.8 years), tertile 2 (n=231; 14.8-17.7 years), and tertile 3 (n=231; 17.8-23.0 years). As part of the PNC, subjects over 10 years old completed a validated self-report regarding their pubertal development; there were no differences in pubertal status between males and females in the third age tertile (80% post-pubertal). We ran SVM with 2F-CV on each tertile separately. Multivariate patterns of topography accurately predicted sex in each of these tertiles. The consistency of results across these tertiles suggests that sex classification based on topography was not impacted by age or pubertal status. To further confirm that results were not driven by pubertal status, we repeated the classification in a subset of the sample composed of just post-pubertal youths.

Next, to ensure that results were not driven by the unequal number of males and females in our sample, we repeated our multivariate analysis on a sex-balanced subsample of 602 subjects: 301 males and 301 randomly selected females. Training and testing subsets within the 2F-CV were also sex-balanced and included 50% males and 50% females. As in our primary analysis, we conducted a chromosomal enrichment analysis to quantify the degree of spatial correspondence between the map of summed absolute prediction weights from this machine

learning model and chromosomal gene sets from the Allen Human Brain Atlas.

We then conducted an additional analysis to ensure that results were not biased by data leakage or use of a population-level template built on data that was not sex-balanced. To address this, we built a group atlas using a sex-balanced group of subjects that was not involved in either model training or testing. First, we randomly selected a sex-balanced group of 346 individuals (173 male and 173 female) from the original sample. Using this group, we created a consensus group atlas (Figure 1a, steps 1-2). Creating the consensus group atlas involves repeating step 1 (Group Atlas Generation) 50 times, with each run including a different subset of 100 subjects. Although each subset of 100 randomly selected individuals was not sex-balanced, subsets were on average sex-balanced across the 50 repeats so the final group atlas was not biased towards either sex (mean 49.62% male, median 50% male, IQR 47-52% male). Next, we used this group atlas to derive individualized networks in the remaining 347 individuals. Finally, we used SVM with nested 2F-CV in this sample of 347 individuals to classify participant sex.

SUPPLEMENTARY TABLES

Network	Number of Vertices
1	6868
2	2967
3	8074
4	1677
5	6037
6	2608
7	4375
8	4776
9	8798
10	1735
11	2412
12	7429
13	1782
14	5557
15	1612
16	5662
17	5699
Total	78068

Table S1. Number of vertices in each network of the consensus group atlas

Sub-class	X-linked genes (N)	X-linked genes
Ast	2	*GPM6B, OPHN1*
Ex1	2	*DIAPH2, GRIA3*
Ex2	0	-
Ex3e	16	*ATP6AP1, ATP6AP2, BEX1, BEX2, BEX4, CDKL5, GDI1, MAP7D2, MORF4L2, NDUFA1, SYN1, SYP, TMSB4X, TSPAN7, TSPYL2, USP11*
Ex5b	2	*DMD, GRIA3*
Ex6b	3	*DMD, GRIA3, PCDH11X*

Table S2. Cell-type sub-classes with expression patterns that correlate with sex differences in topography contain several X-linked genes. Regions exhibiting sex differences in the multivariate pattern of functional topography are enriched in astrocyte-related genes, as well as several excitatory neuron sub-classes, including Ex5b, Ex1, Ex3e, Ex6b, and Ex2. The X-linked genes contained in each of these sub-classes is listed in the table.

SUPPLEMENTARY FIGURES

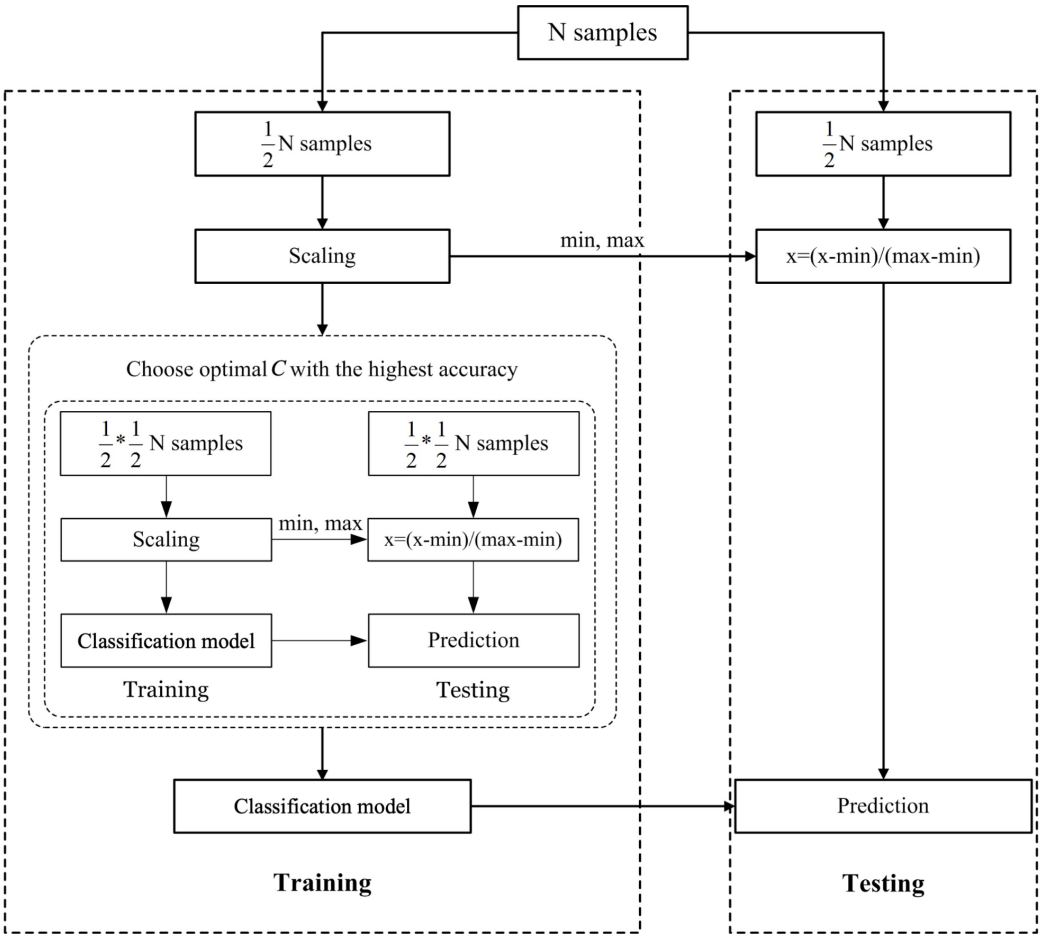

Figure S1. Schematic of one outer loop of the nested 2-fold cross validation (2F-CV) framework. The sample was randomly divided into 2 subsets, with the first half used as a training set and the second half used as a testing set. Each feature was linearly scaled between zero and one across the training dataset; these scaling parameters were applied to the testing sample. An inner 2F-CV was applied within the training set to select the optimal *C* parameter. Based on the optimal *C*, we trained a model using all subjects in the training set, and then used that model to predict the outcome of all participants in the testing set.

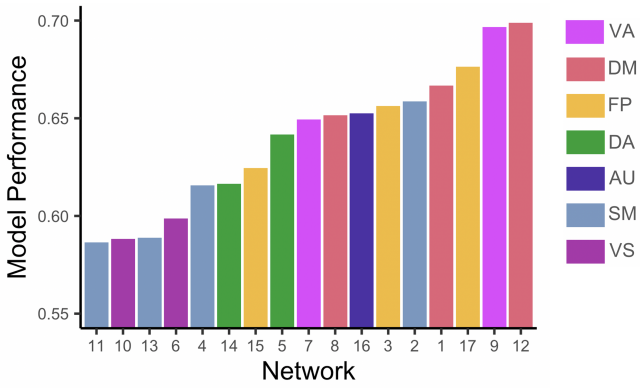

Figure S2. Network-specific multivariate models reveal that topography of association networks most accurately classify participant sex. Although the summed weights depicted in Figure 3C identify which networks contribute most to the prediction, this measure does not directly assess the extent to which each network independently contributes to prediction accuracy. Therefore, we ran 17 network-specific models: for each network, we ran SVM with nested 2F-CV using vertices only from that network. This generated 100 cross-validated prediction scores per network. Bars in the figure represent the average of the 100 cross-validated predictions. These network-specific models revealed that topography of association networks, including the default mode and ventral attention networks, most accurately classified participant sex.

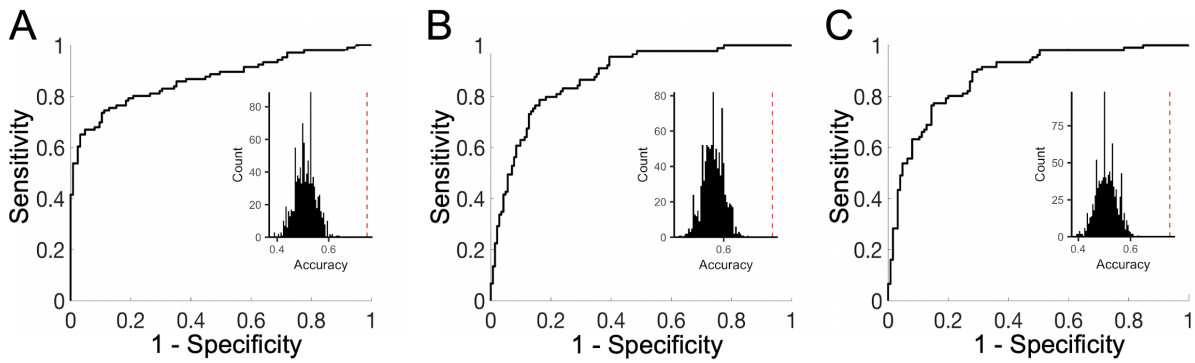

Figure S3. Classification of sex based on multivariate patterns of topography was not impacted by age. We investigated if participant age impacted the ability to classify sex based on multivariate patterns of topography. SVM with nested 2F-CV was used to construct multivariate models that classified participants as male or female in each of three age tertiles. The ROC curves of the resulting models for each tertile are depicted. Inset histogram shows distribution of permuted accuracies. Average accuracy from real (non-permuted) data is represented by the dashed red line. A) In tertile 1, AUC was 0.87; average sensitivity and specificity of the model were 0.65 and 0.83, respectively. Models classified participants as male or female with 74.9% accuracy ($p<0.0001$). B) In tertile 2, AUC was 0.88; average sensitivity and specificity of the model were 0.50 and 0.90, respectively. Models classified participants as male or female with 74.7% accuracy ($p<0.0001$). C) In tertile 3, AUC was 0.88; average sensitivity and specificity of the model were 0.67 and 0.82, respectively. Models classified participants as male or female with 75.0% accuracy ($p<0.0001$).

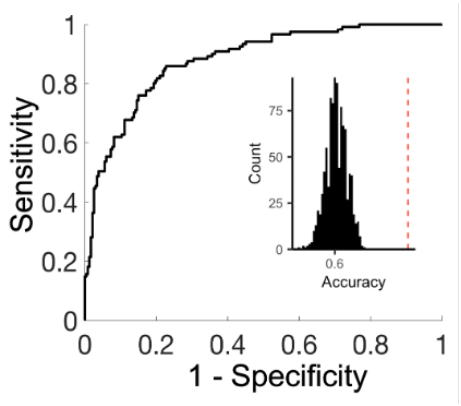

Figure S4. Multivariate pattern analysis using support vector machines predicts subject sex based on functional topography in post-pubertal youths. To ensure that results were not driven by differences in pubertal status, we repeated our multivariate analysis in a subset of the sample composed only of post-pubertal youths. SVM with nested 2F-CV were used to construct multivariate models that classified participants as male or female. The ROC curve of the resulting model is depicted. Area under the ROC curve was 0.88; average sensitivity and specificity of the model were 0.48 and 0.93, respectively. Models classified participants as male or female with 77.3% accuracy. Inset histogram shows distribution of permuted accuracies. The average accuracy of real (non-permuted) data is represented by the dashed red line.

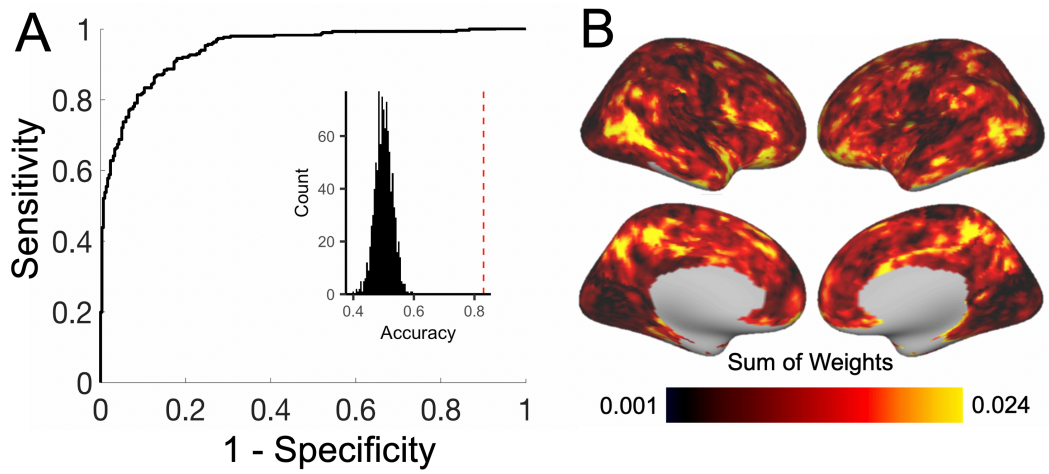

Figure S5. Multivariate pattern analysis using support vector machines predicts subject sex based on functional topography in the sex-balanced subset. A) To ensure that results were not driven by the unequal number of males and females in our sample, we repeated our multivariate analysis on a sex-balanced subsample of 602 subjects: 301 males and 301 randomly selected females. Training and testing subsets within the 2F-CV were also sex-balanced and included 50% males and 50% females. In this sex-balanced subsample, models were able to classify unseen participants as male or female with 83.4% accuracy ($p<0.0001$). Sensitivity and specificity of the model were 0.83 and 0.84, respectively; area under the ROC curve (AUC) was 0.94. The ROC curve of the resulting model is depicted. Inset histogram shows distribution of permuted accuracies. Average accuracy from real (non-permuted) data is represented by the dashed red line. **B)** At each location on the cortex, the absolute contribution weight of each vertex was summed across networks, revealing that association cortex contributed the most to the multivariate model predicting participant sex.

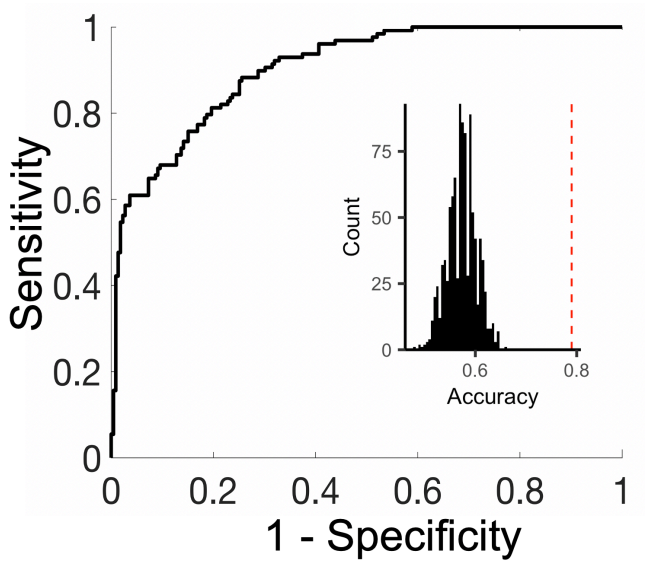

Figure S6. Multivariate pattern analysis using support vector machines predicts subject sex based on functional topography defined with a sex-balanced group atlas. To ensure that results were not driven by potential data leakage resulting from building a group atlas using the entire sample, we built a group atlas using a sex-balanced group of subjects that was not involved in model training and testing. First, we randomly selected a sex-balanced group of 346 individuals (173 male and 173 female). Using this group, we created a consensus group atlas. Next, we used this group atlas to derive individualized networks in the remaining 347 individuals. Finally, we used SVM with nested 2F-CV in this sample of 347 individuals to classify participant sex. Using this approach, we were able to classify subjects as male or female with 79.0% accuracy ($p<0.0001$). Sensitivity and specificity of the model were 0.58 and 0.91, respectively; AUC was 0.90.

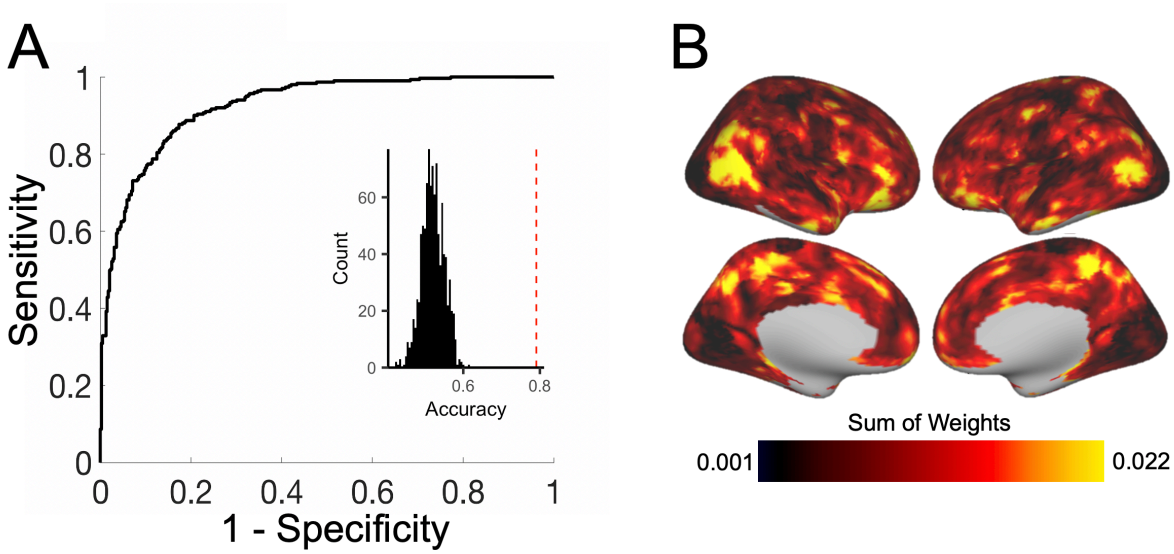

Figure S7. Multivariate pattern analysis following dimensionality reduction predicts subject sex based on functional topography. To ensure that our results were not driven by model-overfitting in the context of an excess number of features, we repeated our multivariate analysis after using principal components analysis (PCA) to reduce the number of features to 100 components. Instead of scaling features between zero and one, features were normalized to a mean of zero and standard deviation of one, as required for PCA. All other SVM parameters were unchanged from our primary analysis. Using this approach, we were able to classify subjects as male or female with 79.1% accuracy ($p<0.0001$). Sensitivity and specificity of the model were 0.73 and 0.84, respectively; AUC was 0.93. The ROC curve of the resulting model is depicted. Inset histogram shows distribution of permuted accuracies. Average accuracy from real (non-permuted) data is represented by the dashed red line. B) At each location on the cortex, the absolute contribution weight of each vertex was summed across networks, revealing that association cortex contributed the most to the multivariate model predicting participant sex.

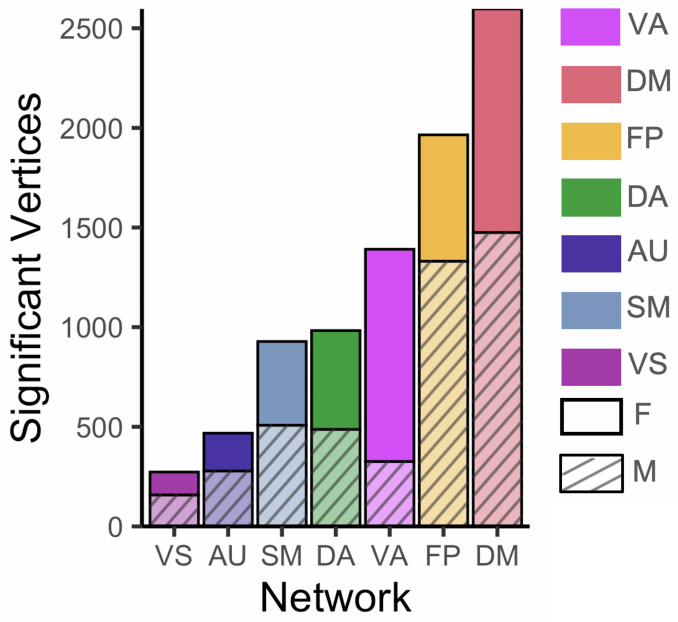

Figure S8. Mass-univariate analyses identify significant sex differences in association networks. A generalized additive model (GAM) was fit at each vertex to evaluate the impact of sex on network loadings. Age (modeled using a penalized spline) and motion were included as covariates. Multiple comparisons within each network were accounted for by controlling the false discovery rate ($Q<0.05$). To identify types of networks with the greatest sex differences, the number of vertices in network type with a significant sex effect was summed separately for males and females (e.g. the DM bar depicted represents the number of vertices with a significant sex effect in networks 1, 8, and 12—the three DM networks). This analysis revealed that sex differences were greatest in association networks.

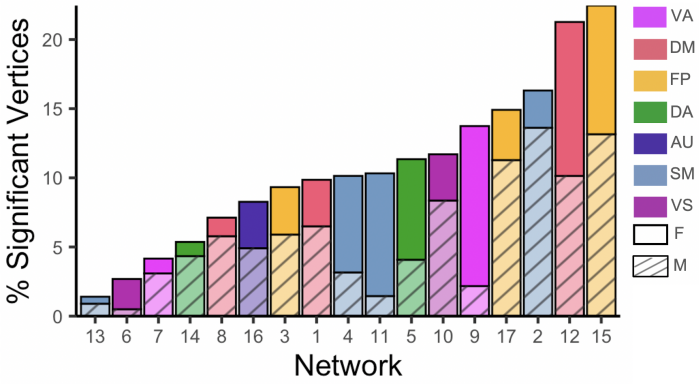

Figure S9. Mass-univariate analyses demonstrate sex differences are greatest in association networks after accounting for network size. A generalized additive model (GAM) was fit at each vertex to evaluate the impact of sex on network loadings. To ensure that results were not driven by network size, after FDR correction across each network, we calculated the percent of vertices in each network that showed a significant sex effect. Solid bars represent the percent of vertices where females had significantly higher loadings than males. Cross-hatched bars represent the percent of vertices where males had significantly higher loadings than females.

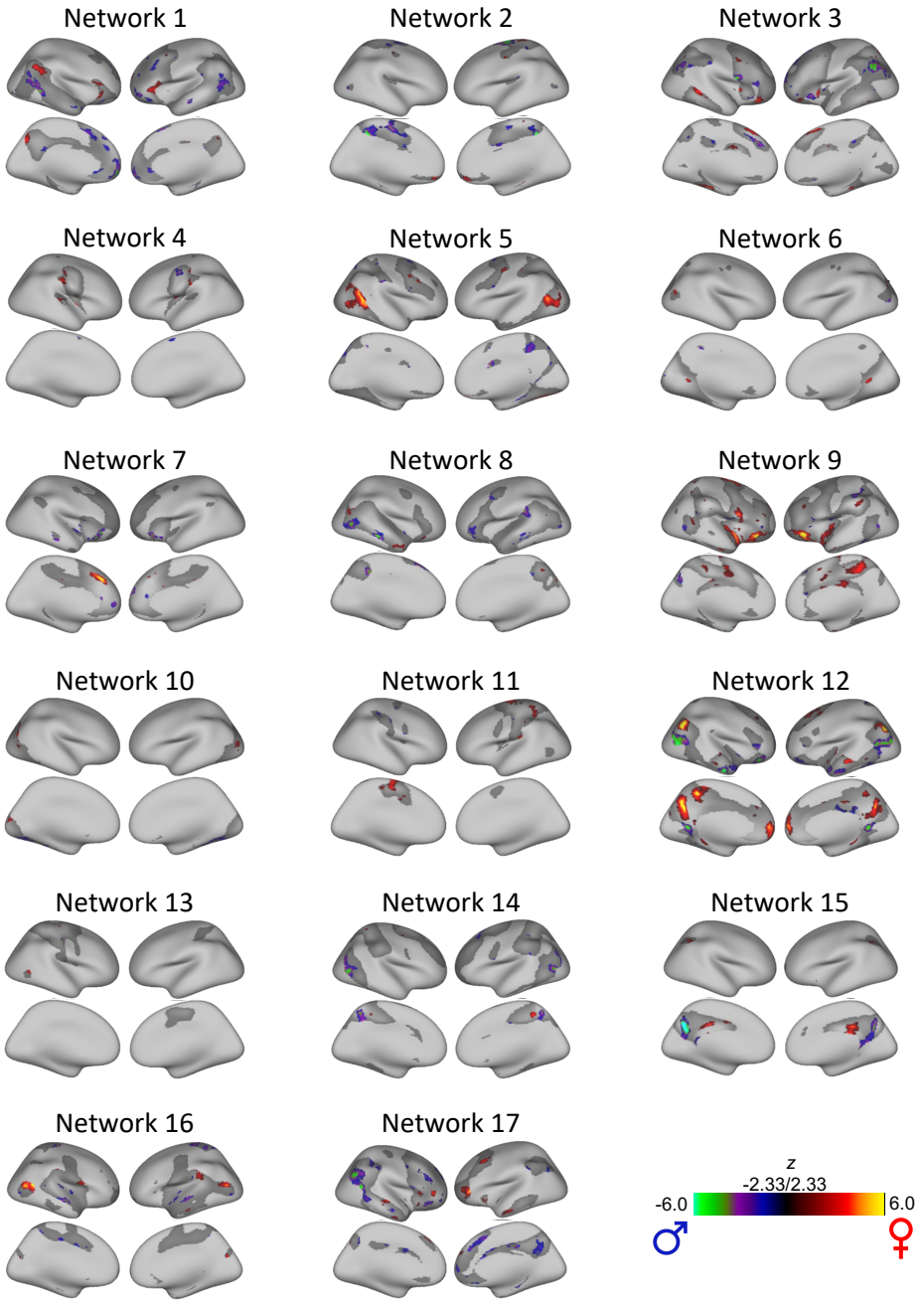

Figure S10. Mass-univariate analyses identify significant sex differences in association networks. A generalized additive model (GAM) was fit at each vertex to evaluate the impact of sex on network loadings. Age (modeled using a penalized spline) and motion were included as covariates. Multiple comparisons within each network were accounted for by controlling the false discovery rate ($Q<0.05$). Significant vertices are displayed for all 17 networks.

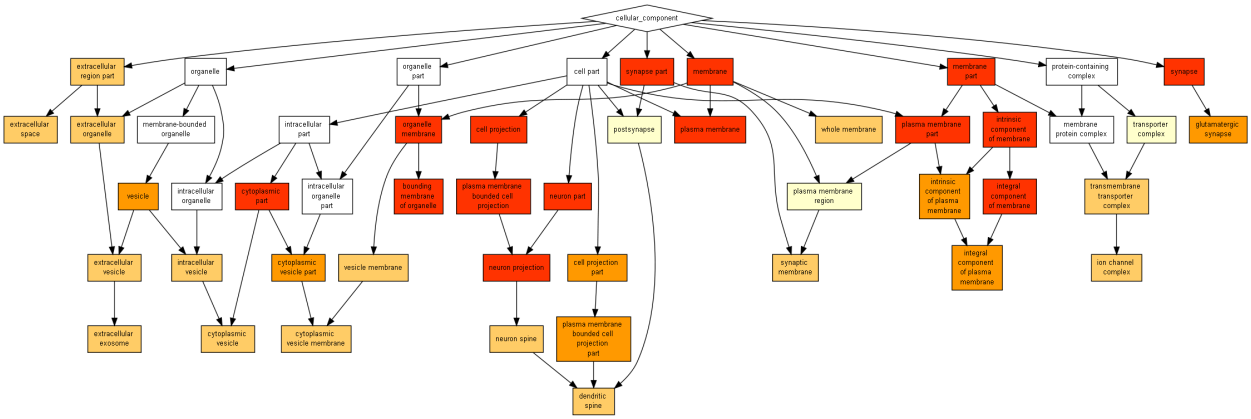

Figure S11. Regions exhibiting sex differences in the multivariate pattern of functional topography are enriched in expression of neuron related genes. We explored whether areas with prominent sex differences in topography show enriched annotation for specific biological processes, cellular components, and molecular functions. We conducted a rank-based gene ontology (GO) enrichment analysis using GOrilla to examine functional enrichment. Full output of cellular component GO terms is depicted. This analysis identified several GO terms relevant to brain anatomy including “neuron part,” “synapse,” and “glutamatergic synapse.”

SUPPLEMENTARY REFERENCES

1. T. D. Satterthwaite *et al.*, Neuroimaging of the Philadelphia neurodevelopmental cohort. *NeuroImage* **86**, 544-553 (2014).
2. T. D. Satterthwaite *et al.*, Functional maturation of the executive system during adolescence. *J Neurosci* **33**, 16249-16261 (2013).
3. D. H. Wolf *et al.*, Functional neuroimaging abnormalities in youth with psychosis spectrum symptoms. *JAMA Psychiatry* **72**, 456-465 (2015).
4. B. Fischl, FreeSurfer. *NeuroImage* **62**, 774-781 (2012).
5. R. Ciric *et al.*, Mitigating head motion artifact in functional connectivity MRI. *Nat Protoc* **13**, 2801-2826 (2018).
6. M. Jenkinson, C. F. Beckmann, T. E. Behrens, M. W. Woolrich, S. M. Smith, FSL. *NeuroImage* **62**, 782-790 (2012).
7. S. M. Smith *et al.*, Advances in functional and structural MR image analysis and implementation as FSL. *NeuroImage* **23 Suppl 1**, S208-219 (2004).
8. R. W. Cox, AFNI: software for analysis and visualization of functional magnetic resonance neuroimages. *Comput Biomed Res* **29**, 162-173 (1996).
9. M. N. Hallquist, K. Hwang, B. Luna, The nuisance of nuisance regression: spectral misspecification in a common approach to resting-state fMRI preprocessing reintroduces noise and obscures functional connectivity. *NeuroImage* **82**, 208-225 (2013).
10. D. A. Fair *et al.*, A method for using blocked and event-related fMRI data to study "resting state" functional connectivity. *NeuroImage* **35**, 396-405 (2007).
11. E. M. Gordon *et al.*, Generation and Evaluation of a Cortical Area Parcellation from Resting-State Correlations. *Cerebral cortex (New York, N.Y. : 1991)* **26**, 288-303 (2016).
12. J. G. Ojemann *et al.*, Anatomic localization and quantitative analysis of gradient refocused echo-planar fMRI susceptibility artifacts. *NeuroImage* **6**, 156-167 (1997).
13. G. S. Wig, T. O. Laumann, S. E. Petersen, An approach for parcellating human cortical areas using resting-state correlations. *NeuroImage* **93 Pt 2**, 276-291 (2014).
14. H. Li, T. D. Satterthwaite, Y. Fan, Large-scale sparse functional networks from resting state fMRI. *NeuroImage* **156**, 1-13 (2017).
15. D. D. Lee, H. S. Seung, Learning the parts of objects by non-negative matrix factorization. *Nature* **401**, 788-791 (1999).
16. A. Sotiras *et al.*, Patterns of coordinated cortical remodeling during adolescence and their associations with functional specialization and evolutionary expansion. *Proc Natl Acad Sci U S A* **114**, 3527-3532 (2017).
17. D. Cai, X. He, J. Han, T. S. Huang, Graph Regularized Nonnegative Matrix Factorization for Data Representation. *IEEE Trans Pattern Anal Mach Intell* **33**, 1548-1560 (2011).
18. R. Kong *et al.*, Spatial Topography of Individual-Specific Cortical Networks Predicts Human Cognition, Personality, and Emotion. *Cerebral cortex (New York, N.Y. : 1991)* **29**, 2533-2551 (2019).
19. D. Wang *et al.*, Parcellating cortical functional networks in individuals. *Nat Neurosci* **18**, 1853-1860 (2015).
20. B. T. Yeo *et al.*, The organization of the human cerebral cortex estimated by intrinsic functional connectivity. *J Neurophysiol* **106**, 1125-1165 (2011).
21. Z. Cui *et al.*, Individual Variation in Functional Topography of Association Networks in Youth. *Neuron* **106**, 340-353.e348 (2020).
22. E. M. Gordon *et al.*, Precision Functional Mapping of Individual Human Brains. *Neuron* **95**, 791-807.e797 (2017).
23. C. Gratton *et al.*, Functional Brain Networks Are Dominated by Stable Group and Individual Factors, Not Cognitive or Daily Variation. *Neuron* **98**, 439-452.e435 (2018).